Scientific Research Publishing

Journal of Power and Energy Engineering, 2026, 14(6), 42-74
https://www.scirp.org/journal/jpee
ISSN Online: 2327-5901
ISSN Print: 2327-588X

Modeling of Intraday Fluctuations in Future Climate Parameters and Their Impact on Perovskite Solar Modules, from a Sustainable Development Perspective

Wakiang Emile Latchiba[1,2*], Sebastian Waita[1], Robert Krueger[2], Julius M. Mwabora[1]

[1]Condensed Matter Research Group, Department of Physics, University of Nairobi, Nairobi, Kenya
[2]Department of Social Science and Policy Studies, Worcester Polytechnic Institute, Worcester, MA, USA
Email: *latchibaemile@gmail.com

How to cite this paper: Latchiba, W.E., Waita, S., Krueger, R. and Mwabora, J.M. (2026) Modeling of Intraday Fluctuations in Future Climate Parameters and Their Impact on Perovskite Solar Modules, from a Sustainable Development Perspective. *Journal of Power and Energy Engineering*, **14**, 42-74.
https://doi.org/10.4236/jpee.2026.146004

Received: May 15, 2026
Accepted: June 27, 2026
Published: June 30, 2026

Abstract

Modeling of intraday fluctuation in future climate parameters. This study uses ARIMA and LSTM models to evaluate and examine the prediction accuracy of four main meteorological parameters (solar irradiance, temperature, relative humidity, and wind speed) that have an impact on perovskite solar modules using Chad as an example. The findings show that the use of averaged climatic data considerably obscures the effects of intraday fluctuation, which significantly increases power output volatility and speeds up degradation. Increasing short-term temperature extremes may further jeopardize system reliability, according to projections under future climate scenarios. The results highlight the necessity of climate-resilient photovoltaic modeling techniques for long-term technological viability and sustainable energy system design. The significance of national and international policy decisions in shaping Chad's demographic, economic, and environmental future is highlighted by these Shared Socioeconomic Pathway projections (SSP1-2.6, SSP2-4.5, SSP3-7.0, SSP4-6.0, and SSP5-8.5). Chad has an important opportunity to pursue a sustainable development pathway that balances economic growth, social equity, and environmental stewardship.

Keywords

Intraday Climate Variability, Perovskite Solar Modules, Future Climate Scenario, Sustainable Development, Climate Change Adaptation in Energy Systems

1. Introduction

To predict the effects of climate change and support sustainable development, it is essential to model intra-annual variations in future climate variables. The most effective methods for capturing these subtle changes include high temporal resolution, physical modeling, artificial intelligence, and dynamic downscaling.

Although perovskite solar modules are a promising technology for renewable energy production, their durability and performance are significantly influenced by climate factors [1]. The efficiency, stability, and longevity of these modules are directly affected by fluctuations in temperature, humidity, and the solar spectrum [2]. The perovskite solar modules experience rapid temperature changes due to changes in ambient temperature and insolation, with gradients of up to 3 K/min and variations of more than 20 K over brief periods [3]. Rapid changes in temperature and solar radiation, for example, can cause the module's temperature to shift dramatically, sometimes by as much as 70˚C. This affects performance and accelerates certain degradation mechanisms [4]. Additionally, heat and humidity together pose significant challenges to cell stability. However, advanced encapsulation techniques may enhance the cells' resistance to hot, humid environments [5].

To predict and optimize the energy performance of perovskite modules under current and future conditions, accurate modeling of climate parameters, including those at the intra-journal scale, is essential [6]. Moreover, studies indicate that adapting module architecture and optimizing materials based on local climate conditions can significantly enhance energy production and durability, resulting in more resilient photovoltaic technologies [7] [8].

Modeling techniques for intrajournalistic fluctuations, physical modeling, and temporal decomposition are essential. The temperature and humidity of the soil can be accurately simulated with high geographic and temporal resolution by utilizing observed climate data and probabilistic forecasts that differ from the hourly scale. Physical models consider the effects of terrain, vegetation, and soil properties when estimating microclimates [9]. Dynamical downscaling and regional climate models (RCMs), such as PRECIS, permit high-resolution simulations of daily maximum temperatures, enhancing the accuracy of local estimates compared to global models [10]. By combining various climate forecasters and scenarios, machine learning techniques, including artificial intelligence (AI) and automatic forest models, as well as explainable models (XAI), are used to predict the volatility of climate variables and their impact on sectors such as energy and tree growth [11]. Variability statistical modeling at the monthly or intra-journal scale supports the representation of changes in the distribution of precipitation or other variables through simple models based on internal climate variability or by pattern scaling approaches [12].

Applications for long-term development, such as managing energy and predicting variations in temperature or solar radiation within journals, help maximize energy use in buildings and enhance renewable energy output [13]. The adaptation of ecosystems and agriculture, combined with high-resolution models, facil-

itates predictions about how ecosystems and cultures respond to extreme climate conditions, streamlining the planning of adaptation measures [14]. By reducing uncertainty through the use of model ensembles and improved observations, we can achieve better quantification of uncertainty, which is crucial for decision-making [15].

To forecast how the temperature of the modules would change in response to ambient temperature and solar radiation, a dynamic iterative model has been developed. By incorporating the device's unique thermal properties, this model enables the extraction of the modules' thermal response to future or extreme climatic circumstances [6].

It is crucial to understand and model these oscillations to predict the longevity and performance of perovskite modules in a climate change context and to develop more resilient photovoltaic solutions. In summary, the proposed title aims to understand and model how intra-journal changes in future climate parameters affect the performance of solar modules made of perovskites while incorporating a long-term development perspective [16]. The main goal is to anticipate and optimize the performance and longevity of perovskite solar modules in the face of rapid and foreseeable climate change.

Accurate long-term prediction of perovskite solar module performance requires accounting for intraday climate variability. Rapid fluctuations in temperature and irradiance can raise module temperature above 70˚C, accelerating degradation [17]. Dynamic modeling captures these thermal responses under future climate scenarios, while global simulations show climate-dependent annual energy yields for tandem perovskite/silicon modules, with uncertainties of about 5% across Köppen-Geiger zones [18]. Optimizing performance also involves adjusting the upper cell gap based on actual weather data, underscoring the importance of a localized and adaptable approach. These studies indicate that considering intra-journal climate variations is vital for maximizing solar energy production, reducing environmental energy consumption, and ensuring the long-term viability of perovskite modules [19]. In addition, to ensure the sustainability and dependability of PSMs in the face of climate change, it is essential to comprehend and model these changes under future climate scenarios.

The effects of climate change are spatially heterogeneous, with high latitudes—especially the Arctic—experiencing magnified temperature rises, and land and polar regions warming more quickly than oceans and coastal areas [20]. Future precipitation patterns will also be unequal, with prolonged droughts in some areas, particularly in mid-latitude and equatorial regions, and increased rainfall and flooding in others [21]. Up to 250 million people in Africa are expected to experience greater drought and water scarcity as a result of these changes, endangering ecosystems, water supplies, and food security [22]. Given the arid circumstances in northern Chad, this backdrop is especially pertinent [23]. The Lake Chad Basin, with its divided northern and southern pools, is a prime example of climatic vulnerability because of the substantial lake shrinkage and increased susceptibility to desiccation caused by rising evaporation, decreased rainfall, and hu-

man water exploitation [24].

High population density along rivers and Lake Chad reflects strong dependence on water resources, making the region highly vulnerable to climate change-induced water scarcity, droughts, and hydrological alterations, with risks of intensified water stress and conflict. Because hourly changes in temperature, solar irradiance, humidity, and wind speed have a significant impact on industries like renewable energy, agriculture, and urban planning, intraday climate modeling is necessary to address these issues. In particular, building energy demand assessment, agricultural water management, and solar energy simulations all depend on precise hourly climatic data [25]. Traditional empirical downscaling techniques are still helpful, but when combined with CMIP6 climate forecasts, hybrid and machine learning techniques—like ARIMA and LSTM—offer more accuracy [26]. The World Climate Research Programme is in charge of CMIP6, which offers standardized climate simulations under Shared Socioeconomic Pathways (SSPs) [27]. These simulations support IPCC AR6 assessments and allow for a thorough assessment of future climate impacts and sustainable development plans [28].

- SSP 1 - 2.6: A scenario with a strong emphasis on climate action and sustainable development.
- SSP 2 - 4.5: Moderate emissions and a middle-of-the-road trend.
- SSP 3 - 7.0: High emissions and regional competition in a fragmented globe.
- SSP 4 - 6.0: Inequality adaptation is difficult.
- SSP 5 - 8.5: A scenario with little migration due to climate change and a high reliance on fossil fuels.

To evaluate the long-term viability of solar systems under extreme climatic scenarios, each Shared Socioeconomic Pathway integrates population, GDP, and CO_2 emissions predictions in line with SDGs 7 (cheap and clean energy) and 13 (climate action). Chad's tremendous solar potential and significant susceptibility to climate extremes make it a case study.

Accurately capturing intraday variability in future climate parameters is crucial for evaluating the performance and sustainability of perovskite solar modules, which are highly sensitive to short-term fluctuations in temperature, irradiance, humidity, and wind. Modeling these dynamics under future scenarios offers insight into stability, degradation risks, and energy yield, particularly in climate-vulnerable regions. Approaching this from a sustainable development perspective supports a comprehensive assessment of technological viability, environmental benefits, and resilience. The next section describes the materials, data, and methods used in this study.

2. Materials and Methods

The materials we used for this study are tandem perovskite-silicon. Under standard test conditions (STC), the efficiency is assumed to be between 25% and 31% [29]. The temperature coefficient is ~−0.25%/˚C, the degradation rate is 1% per

year, and the spectral response is broad, suitable for variable irradiance [30]. A bespoke photovoltaic performance model that included hourly irradiance, temperature, and system losses was used to simulate module performance. We used MATLAB R2024a for time series modeling, ARIMA, LSTM implementation, and plotting. Local computer resources were utilized for the training of deep learning models, such as LSTM. Batch processing and memory optimization were used to handle massive amounts of data.

The Coupled Model Intercomparison Project Phase 6 (CMIP6) climate futures data are widely used to project global climate change under various socioeconomic scenarios. The multi-model CMIP6 ensembles provide an essential foundation for assessing irradiation, temperature, relative humidity, wind speed, extreme events, and other climate variables at the global, national (in the case of Chad), and regional levels. A federated organization, CMIP6 combines collective experiences with thematic projects to address a variety of scientific topics. The introduction of new socioeconomic scenarios (SSP) and standardized protocols for climate, carbon cycle, and global climate modeling [31].

With results showing a potential increase in global temperatures of around 1.5˚C in the most pessimistic scenarios (SSP 5 - 8.5) compared to CMIP5, the CMIP6 estimates cover a wide range of emission scenarios. The benefits of attenuation are readily apparent when comparing the SSP scenarios, and in some scenarios, internal variability tends to decrease over the century.

Statistical and empirical methods—these techniques involve fitting functional forms to historical hourly observations. Sinusoidal models, for instance, use a sine wave to represent the solar irradiance, temperature, relative humidity, and wind speed throughout the day [32].

$$I(t) = I_{Max} \cdot \sin\left[\frac{\pi(t - t_{Sunrise})}{t_{Sunset} - t_{Sunrise}}\right] \quad \text{for} \quad t_{Sunrise} \le t \le t_{Sunset} \tag{1}$$

where:

$I(t)$: irradiance at hour *t*.

I_{Max} : Maximum irradiance (often ~daily GHI/5).

$t_{Sunrise} = 6$, $t_{Sunset} = 18$ (for simplicity).

$$T(hr) = T_{Min} + (T_{Max} - T_{Min}) \cdot \sin\left[\frac{\pi(h - h_{Sunrise})}{h_{Sunset} - h_{Sunrise}}\right] \tag{2}$$

$$RH(t) = RH_{Mean} + A \cdot \cos\left[\frac{2\pi(t - t_{Peak})}{24}\right] \tag{3}$$

where:

RH_{Mean} : Average daily humidity.

A : Amplitude (e.g., 10% - 20%).

t_{Peak} : Time when RH is maximum (usually around 5 AM).

$$W(t) = W_{Mean} + A \cdot \sin\left[\frac{2\pi(t - t_{Max})}{24}\right] \tag{4}$$

where:

W_{Mean} : Average daily wind speed.

A : Amplitude (variation of wind during the day).

t_{Max} : Hour of peak wind speed (e.g., 14 or 15 h).

Mathematical modeling of the different models used (ARIMA and LSTM) for forecasting the climate parameters [33]. The general ARIMA model is given by Equation (5).

$$\phi(B)(1-B)^{d} y_{time} = \theta(B)\varepsilon_{white\ noise} \tag{5}$$

where:

y_{time} : original time series at time t.

B : Backward shift operator ($By_{time} = y_{t-1} or$).

d : order of differencing.

$\phi(B)$: autoregression (AR) polynomial of order p.

$\theta(B)$: moving average (MA) polynomial of order q.

$\varepsilon_{white\ noise}$: error term.

After differencing d times:

$$y'_t = \phi_1 y'_{t-1} + \phi_2 y'_{t-2} + \cdots + \phi_p y'_{t-p} + \theta_1 \varepsilon_{t-1} + \cdots + \theta_q \varepsilon_{t-q} \tag{6}$$

where:

$$y'_t = (1-B)^{d} y_t \tag{7}$$

For ARIMA (1, 1, 1):

$$y_t - y_{t-1} = \phi_1 (y_{t-1} - y_{t-2}) + \varepsilon_t + \theta_1 \varepsilon_{t-1} \tag{8}$$

The mathematical model of the LSTM (Long Short-Term Memory) model is given by Equations (9) to (14).

Forget the gate.

$$f_t = \sigma\left[W_f \cdot (h_{t-1}, x_t) + b_f\right] \tag{9}$$

$$\text{Input gate: } i_t = \sigma\left[W_i \cdot (h_{t-1}, x_t) + b_i\right] \tag{10}$$

$$\tilde{C}_t = \tanh\left[W_c \cdot (h_{t-1}, x_t) + b_c\right] \tag{11}$$

$$\text{Cell state update: } C_t = f_t \odot C_{t-1} + i_t \odot \tilde{C}_t \tag{12}$$

$$\text{Output gate: } O_t = \sigma\left[W_O \cdot (h_{t-1}, x_t) + b_O\right] \tag{13}$$

$$\text{Final output: } h_t = O_t \odot \tanh(C_t) \tag{14}$$

where:

x_t : input at time t.

h_t : hidden state.

C_t : Cell state.

σ : sigmoid activation.

tan$h$: hyperbolic tangent activation.

$\odot$: element-wise multiplication.

W : and b : weight matrices and biases.

Table 1 shows the key points for these two models.

Table 1. Comparison models.

Feature	ARIMA	LSTM
Type	Linear, statistical	Nonlinear neural network
Inputs	Past values, lags	Past values, sequences
Forecasting	Short- to medium-term	Short- to long-term
Stationarity	Requires stationery	Can learn from raw nonstationary
Multiple vars	No (ARIMAX needed)	Yes (multivariate LSTM)

The mathematical model of evaluation indicators [34] is given by the Equations (15), (16), and (17).

$$\mathrm{RMSE} = \sqrt{\frac{1}{n}\sum_{i=1}^{n}\left(y_i - \tilde{y}_t\right)^2} \tag{15}$$

$$\mathrm{MAE} = \frac{1}{n}\sum_{i=1}^{n}\left|y_i - \tilde{y}_t\right| \tag{16}$$

$$\mathrm{MAPE} = \frac{100\%}{n}\sum_{t=1}^{n}\left|\frac{y_t - \tilde{y}_t}{y_t}\right| \tag{17}$$

where:

y_t : actual value at time t.

$\tilde{y}_t$: predicted value at time t.

n: number of observations.

- Data and climate scenarios

Using specific global climate models (GCMs) under the shared socioeconomic pathway (SSP) scenarios SSP 1 - 2.6, SSP 2 - 4.5, SSP 3 - 7.0, SSP 4 - 6.0, and SSP 5 - 8.5, climate forecasts were derived from coupled Model Intercomparison Project phase 6 (CMIP6) datasets. For both the historical baseline period (1985-2014) and the future projection period (2025-2100), daily climatic variables for Chad were collected, including near-surface air temperature, surface solar radiation, relative humidity, and wind speed. After regridding and downscaling, the analysis employed a spatial resolution of roughly 0.25˚ × 0.25˚. N'Djamena and other significant climatic zones were among the representative locations in Chad for which climate data were retrieved. To increase the consistency between the modeled and actual climate conditions, bias correction and statistical downscaling approaches were used. The SSP public database and associated worldwide climate scenario archives included socioeconomic metrics, such as SSP-based population, GDP, and CO_2 emission trajectories for Chad.

- Time-series preparation and data splitting

The time-series data were arranged using a sliding window method with 100 time steps for each of the climatic variables (solar irradiance, temperature, relative

humidity, and wind speed). The 100 time steps are 100 consecutive historical observations that are utilized as input sequences to forecast the series' next value. With this method, temporal dependencies and short-term climate variability patterns pertinent to photovoltaic system performance can be captured by the ARIMA and LSTM models.

Before modeling, each variable's dataset was standardized and split into three parts: 70% for training, 15% for validation, and 15% for testing. The models were fitted using the training dataset; overfitting control and hyperparameter tuning were done using the validation dataset, and the testing dataset was set aside for the final performance assessment. In order to preserve the temporal integrity of the time-series forecasting process, the data splitting maintained the chronological order of the climate datasets.

- Forecasting Model configuration

To guarantee stationarity and reduce residual errors, ARIMA models were applied independently to each meteorological variable. The best (p, d, q) orders were chosen using the Akaike Information Criterion (AIC), differencing, and autocorrelation diagnostics.

Sequences of 100 time steps were used as inputs to the LSTM model to forecast the next observation. The network consisted of one 50-unit LSTM layer and a dense output layer. It was trained for 100 epochs using the Adam optimizer and the Mean Squared Error (MSE) loss function.

The datasets were temporally separated into training, validation, and testing subsets after all variables were adjusted to the range [0,1] using Min-Max scaling before training.

3. Results and Discussion

3.1. ARIMA and LSTM Model

3.1.1. Autoregressive Integrated Moving Average Model

A mathematical model called the Autoregressive Integrated Moving Average (ARIMA) method is used in time series modeling and forecasting. The Box-Jenkins approach forms the foundation of the ARIMA model. It includes moving average (MA) and autoregression (AR) models. According to the AR model, the current observation in the time series is a linear combination of previous observations plus a noise term.

Figure 1(a) shows the observed and forecasted irradiance (in W/m^2) over 100 time steps, with the forecast generated using an ARIMA model. Below the title, three performance metrics for the ARIMA forecast are provided: The RMSE (root mean square error) of 53.27 indicates the average size of the errors. A lower RMSE signifies a better fit. The average magnitude of the mistakes is likewise measured by the MAE (mean absolute error) of 47.05, but it does not square them. A lower MAE is preferable to a lower RMSE. The accuracy is expressed as a percentage of the error about the actual numbers, with an MAPE (mean absolute percentage

error) of 9.4%. The forecast typically deviates from the observed values by 9.4%, according to an MAPE of 9.4%. Blue solid line: Observed data. The actual irradiance values across the 100 time steps are displayed in this line. It shows notable oscillations, suggesting that solar irradiance is dynamic. There seem to be some overarching patterns, including an initial rise, a subsequent decline, and then an additional rise in the last stages. The observed values are approximately between 400 W/m^2 and 600 W/m^2. The straight, horizontal, red dashed line that represents the ARIMA forecast shows a consistent expected value (about 560 - 570 W/m^2) for each of 100 time steps. This implies that the trained or configured ARIMA model is either predicting a persistence value or a long-term average and is not able to grasp the dynamics.

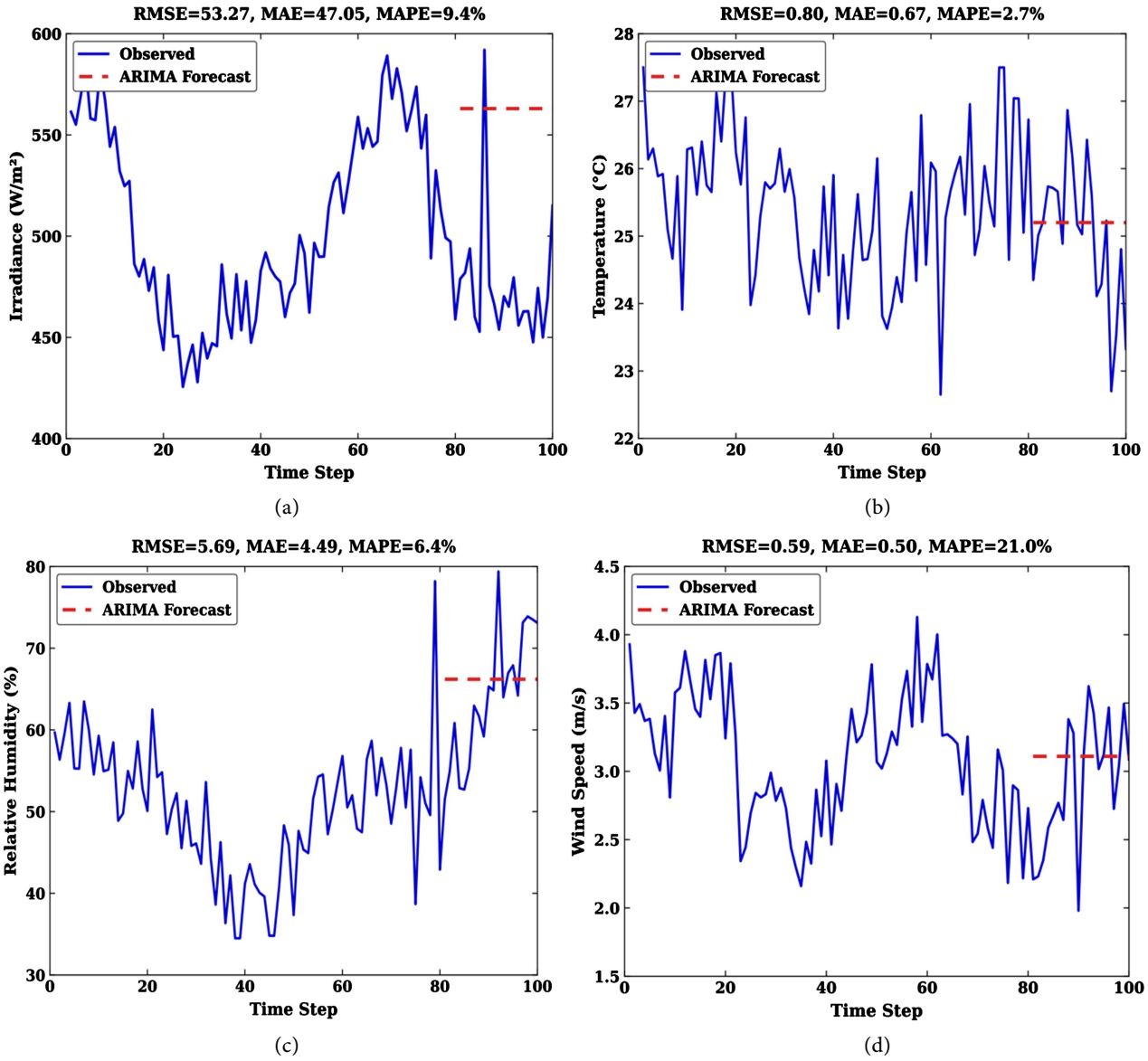

Figure 1. Autoregressive integrated moving average model for climate variable. (a) Irradiance; (b) Temperature; (c) Relative humidity; (d) Wind speed.

The variable observed irradiance differs greatly from the constant ARIMA forecast. The RMSE and MAE values, which are comparatively high considering the range of the irradiance values, show this disparity. This is further quantified by the MAPE of 9.4%, which shows a discernible percentage error.

In summary, Figure 1(a) shows the irradiance forecast using an ARIMA model. The visual representation shows that the ARIMA model in this case is generating a steady forecast, missing the dynamic fluctuations shown in the real irradiance data. Even though the metrics offer a quantitative estimate of error, this shows that either a different forecasting model would be more suitable for this specific irradiance time series, or the model might require additional refining or re-parametrization.

Figure 1(b) shows the observed and forecasted temperature (in ˚C) over 100 time steps, with the forecast generated using an ARIMA model. Below the title, three performance metrics for the ARIMA forecast are provided: RMSE = 0.80, which measures the average error magnitude. A lower RMSE indicates a better fit. MAE = 0.67 also measures the average error magnitude, with a smaller MAE being preferable. MAPE = 2.7%, relates to the actual values, and represents the accuracy as a percentage of error. An average deviation of 2.7% between the forecast and observed values is indicated by an MAPE of 2.7%. The blue line shows the actual temperature values over the 100 time steps. Variations over time are indicated by the notable fluctuations in the recorded temperature. With some maxima topping 28˚C, the values typically fall between roughly 23˚C and 27˚C. The ARIMA forecast (red dashed line) represents the predictions made by the ARIMA model. The ARIMA forecast in this case is a straight, horizontal dashed line that begins at time step 80 and extends to time step 100, in contrast to the preceding irradiance chart. This implies that after being trained on data up to time step 80, the model is making a multi-step-ahead forecast for the remaining portion of the time series. This forecast constant nature means that the ARIMA model forecasts a stable temperature of between 25˚C and 25.5˚C for the anticipated period (time steps 80 - 100).

Despite smoothing out the short-term fluctuations, the ARIMA model offers a somewhat accurate forecast for temperature, at least in terms of overall magnitude, as evidenced by the low RMSE (0.80), MAE (0.67), and particularly MAPE (2.7%). Generally speaking, a forecasting accuracy of 2.7% is regarded as good.

Figure 1(b), in summary, shows the temperature prediction of an ARIMA model. The latter portion of the time series (from time step 80 onwards) seems to be consistently predicted by the model several steps ahead of time. Although the prediction does not account for high-frequency variations, its performance measures (RMSE, MAE, and MAPE) indicate that it is reasonably accurate in predicting the overall temperature. Due to either improved model tuning or the intrinsic properties of the temperature time series, this ARIMA model seems to be more successful in forecasting temperature than the one previously demonstrated for irradiance.

Figure 1(c) shows the observed and forecasted relative humidity (in %) over

100 time steps, with the forecast generated using an ARIMA model. Three performance metrics for the ARIMA forecast are RMSE = 5.69 and MAE = 4.49, both of which measure the average magnitude of the errors, and MAPE = 6.4%, which indicates the accuracy of the actual numbers as a percentage of the inaccuracy. An average deviation of 6.4% between the forecast and observed values is reflected by an MAPE of 6.4%. The observed data (the blue solid line) shows the actual relative humidity values over the 100 time steps. The observed relative humidity fluctuates significantly. There is a clear pattern: higher humidity (around 60% - 70%) at the beginning of the observed period, followed by a drop to lower humidity (often below 40%) between time steps 40 - 60, then a rebound to higher humidity (typically above 70%, with peaks near 80%) towards the end of the observed period. The red dashed line represents the predictions made by the ARIMA model. Here, the ARIMA forecast is shown as a straight, horizontal dashed line that begins at time step 80 and extends to time step 100, similar to the temperature figure. This indicates that, after being trained on data up to time step 80, the forecast for the remaining portion of the time series is multi-step ahead. The constant character of this forecast suggests that the ARIMA model predicts a stable relative humidity value, most likely between 66 and 67 percent, during the period (time steps 80 - 100). The performance of an ARIMA model in predicting relative humidity is depicted in the figure.

Figure 1(d) presents a comparison between observed wind speed data and the wind speed forecast generated by an ARIMA model. The accuracy metrics for the ARIMA forecast are provided: RMSE (Root Mean Square Error) = 0.59, MAE (Mean Absolute Error) = 0.50, and MAPE (Mean Absolute Percentage Error) = 21.0%. The model's performance is measured by these metrics, where higher accuracy is typically indicated by lower numbers. Depending on the application, a mean absolute deviation (MAPE) of 21.0% indicates that the forecast typically deviates by 21% from the observed data. Throughout the duration, there are notable variations in the observed wind speed. It typically exhibits distinct peaks and troughs and ranges between around 2.0 m/s and 4.0 m/s. There are intervals of reduced wind speed, especially around time step 40 and between time steps 70 and 80, as well as a noticeable peak at time step 60, reaching over 4.0 m/s. Only the latter portion of the time series, between time steps 80 and 100, is displayed with the ARIMA forecast. This suggests that the model was most likely utilized for forecasting after being trained on the prior data. The ARIMA projection is a very flat line that hovers slightly over 3.0 m/s (around 3.1 m/s) during the forecast period. It implies that for the prediction horizon, the model forecasts a constant wind speed in this range. The ARIMA model gives a general average when compared to the observed data in the forecast zone, but it is unable to account for the notable oscillations and overall downward trend in the recorded wind speed from time step 80 to 100.

Figure 1(d) shows the attempt to predict wind speed using the ARIMA model. The visual comparison highlights the model's shortcomings, especially in captur-

ing the volatility and particular trends of the measured wind speed, especially during the forecast period, even though the model produces a forecast with particular error metrics. The forecast produced by the ARIMA model is smoothed out and does not accurately capture the dynamic nature of the observed wind speed. The finding that the predicted and observed values differ noticeably is quantitatively supported by the MAPE of 21%. Table 2 presents the main meteorological parameters, evaluation indicators, and numerical values.

Table 2. Recap of evaluation indicators.

Meteorological parameters	Evaluation indicators	Numerical value
Solar irradiance	RMSE	53.27
	MAE	47.05
	MAPE	9.4%
Temperature	RMSE	0.80
	MAE	0.67
	MAPE	2.7%
Relative humidity	RMSE	5.69
	MAE	4.49
	MAPE	6.4%
Wind speed	RMSE	0.59
	MAE	0.50
	MAPE	21.0%

Based on Figure 1, a popular and proven statistical method for predicting time series, including climate factors, is the ARIMA model. ARIMA models are excellent at identifying patterns, seasonality, and linear relationships in the historical data of a single variable. However, they can be limited in their ability to reliably forecast highly dynamic and non-linear climate characteristics, as seen in the figures supplied. Although the model's performance may be numerically evaluated using the quantitative metrics (RMSE, MAE, and MAPE) as shown in Table 2, the visual comparison frequently reveals that the ARIMA forecast may appear unduly stable or flat during times when the observed data exhibits notable variability. This implies that although ARIMA can offer a baseline forecast, it might not adequately account for the intricate, possibly non-linear relationships and outside influences that affect climate variables. To address the limitation of ARIMA, let's apply the LSTM model for non-linearity.

3.1.2. Long Short-Term Memory Models

According to the main advantages of the LSTM (Long Short-Term Memory) model over ARIMA for climate data, they capture non-linear relationships, handle long-term dependencies, and naturally extend to multivariate forecasting.

Figure 2(a) presents a comparison between observed solar irradiance data and a forecast generated by a Long Short-Term Memory (LSTM) model. Observed data (solid blue line) presents the actual, measured irradiance values over the full 100 time steps. The data fluctuates between about 420 W/m^2 and 600 W/m^2, demonstrating high instability. The LSTM forecast red line presents the predictions made by the LSTM model. A forecast horizon (probably a multi-step-ahead projection) is indicated by the fact that the forecast is only displayed for the last segment of the time series, beginning at time step 80. Three important metrics, usually computed across the forecast period (time steps 80 - 100), are included in the figure to evaluate the accuracy of the LSTM forecast: RMSE = 32.81, MAE = 26.91, and MAPE = 5.3%. Throughout the forecast period, these metrics show the overall accuracy and size of the error between the observed values and the LSTM's predictions. An MAPE of 5.3% indicates that, on average, the model's predictions during that time period differ by roughly 5.3% from the actual values.

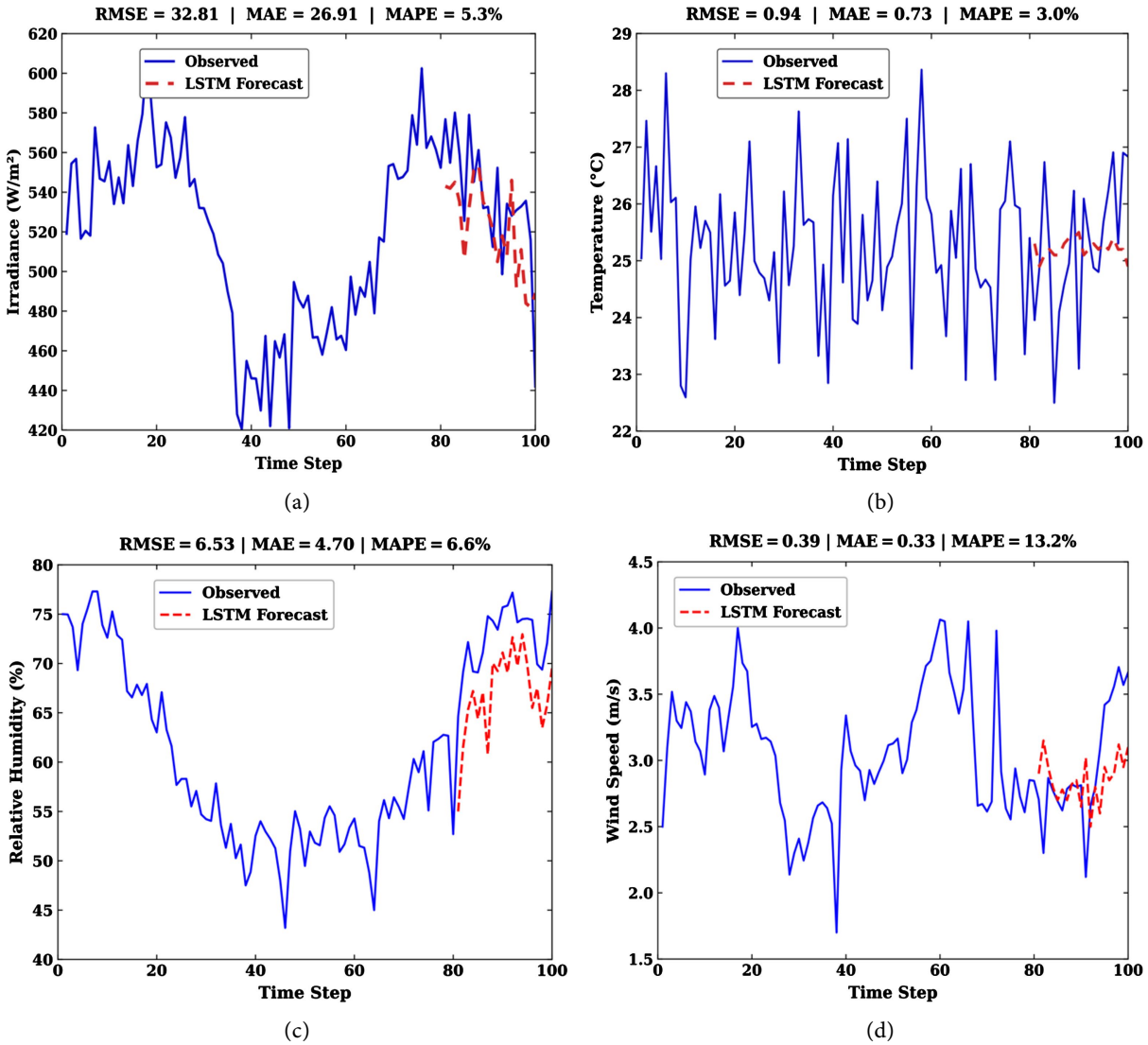

Figure 2. Long short-term memory models. (a) Irradiance; (b) Temperature; (c) Relative humidity; (d) Wind speed.

In summary, the figure shows a time series forecasting scenario for solar irradiance using an LSTM model. It includes quantitative error metrics and a visual comparison of predicted and actual values. This figure visually demonstrates the LSTM model's ability to capture the trend of the irradiance data during the final 20 time steps.

Figure 2(b) illustrates a comparison between observed temperature data and temperature forecasts generated by an LSTM (long short-term memory) model. Observed data in the blue line represents the actual measured temperature values over the entire 100 time steps. The data seems to vary a lot, roughly between 23 and 28 degrees Celsius. The LSTM forecast in the dashed red line displays the LSTM model's temperature forecasts. The forecast is shown for the later portion of the time series, roughly from time step 80 to 100, demonstrating a multi-step-ahead forecasting horizon, just like in the preceding picture. The metrics are shown in the figure. These measures show how much the actual measured temperatures during the forecast period differed from the forecasts made by the LSTM. An average deviation of 3.0% between the model's predictions and the actual temperature values is shown by an MAPE of 3.0%. Given the range of temperature variation, the RMSE and MAE values are comparatively low, indicating good accuracy.

In conclusion, this graphic illustrates how well an LSTM model predicts extremely erratic temperature data. The numeric error metrics and the visual depiction both indicate that the model does a good job of forecasting future temperature values over the given forecast horizon.

Figure 2(c) presents the relative humidity. The blue represents the actual measured relative humidity values across all 100 time steps. Significant variations can be seen in the data, which typically range between 45% and 75%. There appears to be a pattern where humidity is high at the beginning, drops off somewhat by time step 40 - 50, and then increases once again in the final stages. The dashed red line represents the predictions made by the LSTM model. The forecast, which represents the model's multi-step-ahead prediction horizon, is displayed for the last segment of the time series, roughly from time step 80 to 100, much like the earlier numbers. Three quantitative measures, computed across the forecast period (time steps 80 - 100), are included in the figure to assess the accuracy of the LSTM forecast: RMSE = 6.53, MAE = 4.70, and MAPE = 6.6%. These measurements show how much the actual observed relative humidity during the forecast period differed from the LSTM's predictions. An average deviation of 6.6% between the model's predictions and the actual relative humidity measurements is shown by an MAPE of 6.6%.

In conclusion, this graph shows how well the LSTM model predicts relative humidity. The model's capacity to accurately follow the abrupt, fast changes is limited, resulting in a tiny error percentage, even though it properly catches the overall increasing trend in the latter portion of the data.

Figure 2(d) displays a comparison between observed wind speed data and fore-

casts generated by an LSTM model. The solid blue line represents actual measured wind speed values over the entire 100 time steps. There are notable short-term variations in the data, which typically range from about 1.7 m/s to 4.1 m/s. There are constant, quick shifts rather than a discernible long-term pattern. The dashed red line represents the predictions made by the LSTM model. The forecast is displayed for the last segment of the time series, from about time step 80 to 100, illustrating the model's multi-step-ahead prediction horizon, much like in the earlier plots in this series. The measurements show how much the actual measured wind speed during the forecast period differed from the LSTM's predictions. With the greatest MAPE of 13.2% among the four variables (wind speed, temperature, relative humidity, and irradiance), it indicates that, on average, the model's predictions differ by 13.2% from the actual wind speed values.

In summary, this graph highlights how challenging it is to predict highly variable wind speed data. Compared to other meteorological factors in the series, the significant short-term fluctuations in wind speed result in a slightly higher prediction error (13.2% MAPE), even though the LSTM model generally produces a forecast that aligns with the observed pattern. Table 3 presents the recap of the final evaluation indicators.

Table 3. Recap of the final evaluation indicators.

Meteorological parameters	Evaluation indicators	Numerical value
Solar irradiance	RMSE	32.81
	MAE	26.91
	MAPE	5.3%
Temperature	RMSE	0.94
	MAE	0.73
	MAPE	3.0%
Relative humidity	RMSE	6.53
	MAE	4.70
	MAPE	6.6%
Wind speed	RMSE	0.39
	MAE	0.33
	MAPE	13.2%

For variables with less extreme, rapid oscillations and clearer underlying patterns, such as temperature and irradiance, the LSTM model performs well, making it a useful tool for weather forecasting. However, as the variable's inherent volatility and unpredictability increase (as with relative humidity and especially wind speed), its accuracy decreases.

3.1.3. Comparison of ARIMA and LSTM Models

The comparative analysis indicates that model performance depends on the meteorological variable being forecasted. The LSTM model demonstrated its capacity

to capture nonlinear patterns and temporal dependences in solar irradiance and wind speed by achieving superior accuracy based on the evaluation metrics (RMSE, MAE, and MAPE). For temperature and relative humidity, on the other hand, ARIMA showed somewhat fewer prediction errors, indicating that. These variables have temporal features that are well represented by linear statistical models. Overall, neither model consistently performed better than the other across all variables; instead, the relative performance of the two models varied according to the features of the climate parameter under study.

Figure 3(a) displays a comparison of observed solar irradiance data with forecasts generated by two different models: an ARIMA (Autoregressive Integrated Moving Average) model and an LSTM (Long Short-Term Memory) model. By contrasting their performance with. The observed data and the graph graphically illustrate how the ARIMA and LSTM models try to predict irradiance during the last 20 time steps. In this particular irradiance projection period, LSTM performs noticeably better than ARIMA. When the trend changes, ARIMA's forecast, which is incredibly stable and nearly flat, rapidly deviates from the actual data. LSTM is far more flexible in responding to the shifting dynamic of the irradiance data, especially the notable decline near the conclusion of the series, thanks to its capacity to learn intricate non-linear patterns and temporal connections.

To sum up, this image illustrates how an LSTM model is superior to a conventional ARIMA model for predicting solar irradiance when the underlying patterns include notable non-linearity or sudden trend changes. The LSTM model exhibits a better capacity to capture and forecast these more intricate behaviors, whereas the ARIMA model, which most likely relies on linear assumptions, is unable to adjust to the shifting dynamics.

Figure 3(b) illustrates a comparison of observed temperature data with forecasts generated by two different models: an ARIMA model and an LSTM model. Both ARIMA and LSTM forecasts do comparably well in capturing the overall level of temperature for this particular dataset, but they are unable to accurately predict the significant short-term volatility shown in the observed data. Compared to irradiance, the visual difference between ARIMA and LSTM forecasts is less noticeable here. Neither model fully accounts for the abrupt, real-time temperature changes, even though the LSTM may exhibit a somewhat better fit in certain microtrends. This implies that either the high-frequency fluctuation of the temperature data is just hard to anticipate several steps ahead of time or that it is intrinsically very noisy or influenced by causes not fully represented by either model's learned patterns.

Although both the ARIMA and LSTM models offer decent smoothed forecasts that capture the overall average for this extremely variable temperature dataset, they both struggle to accurately predict the abrupt, high-frequency variations. The advantages of the LSTM's non-linear capabilities are less noticeable in this case than in the irradiance example, indicating that both models encounter comparable difficulties for this particular kind of short-term temperature variability.

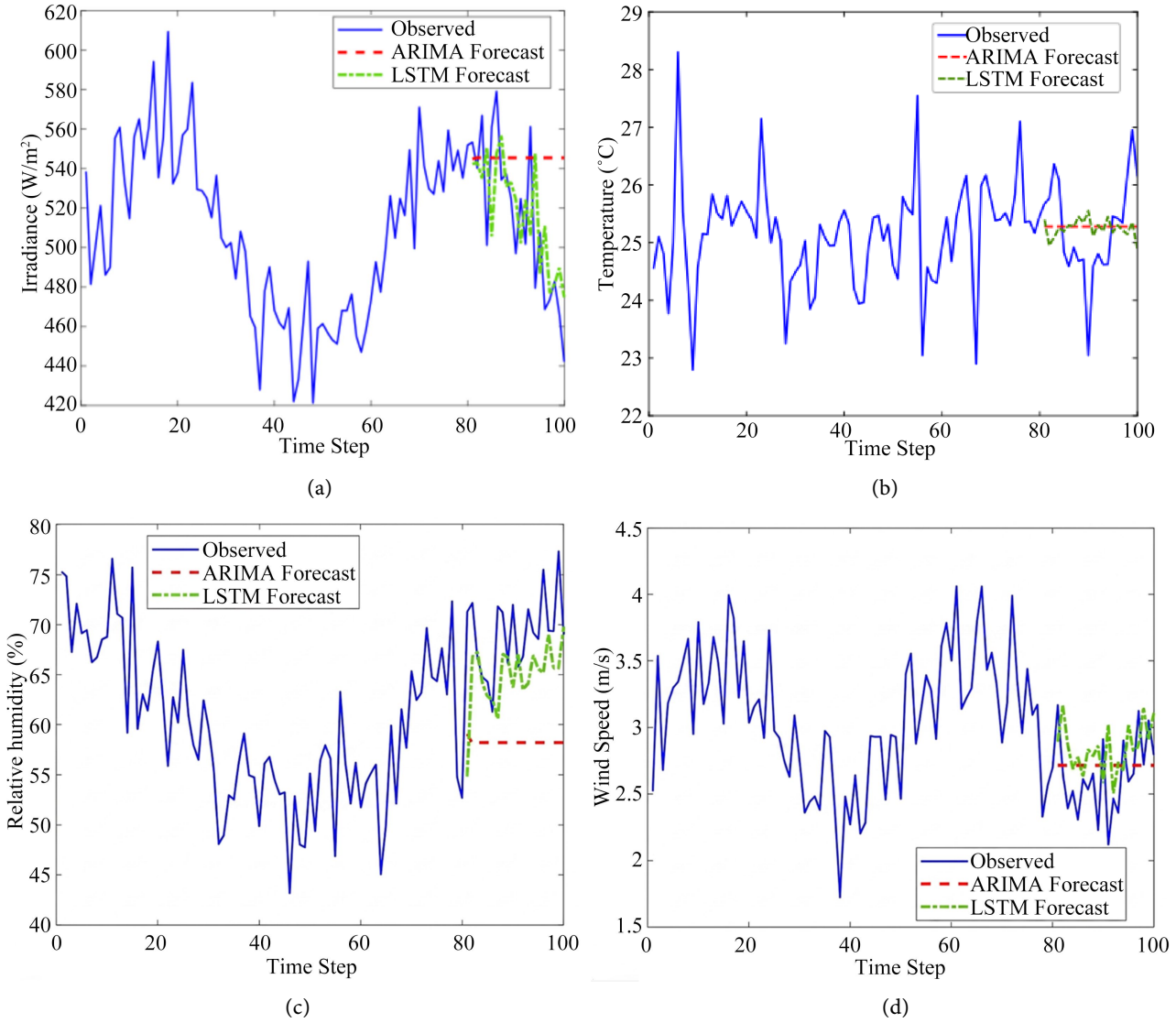

Figure 3. Comparison of ARIMA to LSTM models. (a) Irradiance; (b) Temperature; (c) Relative humidity; (d) Wind speed.

Figure 3(c) presents a comparison of observed relative humidity data with forecasts generated by ARIMA and LSTM models. For relative humidity forecasting in this period, the LSTM model clearly and substantially outperforms the ARIMA model. The flat forecast from the ARIMA model suggests that it was unable to adjust to the volatility or the growing trend. This could be because of its intrinsic linearity, which makes it difficult to deal with non-linear or quickly shifting relative humidity patterns. The LSTM model is preferable in this instance because it uses its capacity to learn intricate patterns and long-term relationships to make a far more accurate prediction of the future relative humidity.

This picture indicates that the LSTM model is significantly more successful than a standard ARIMA model at producing accurate forecasts for relative humidity data, particularly when the data shows complex trends and high short-term variability. The flat and erroneous prediction of the ARIMA model demonstrates its

shortcomings in capturing dynamic, non-linear processes.

Figure 3(d) presents a comparison of observed wind speed data with forecasts generated by ARIMA and LSTM models. The LSTM model performs noticeably better than the ARIMA model when it comes to wind speed forecasting. The extremely non-linear and chaotic behavior of wind speed is beyond the linear character of the ARIMA model. Despite the inherent difficulties of predicting such a chaotic variable, the LSTM model is far more effective at tracking the dynamic and volatile character of wind speed because of its ability to acquire complex temporal relationships and non-linear patterns. The movements of the observed data are clearly more in line with the LSTM forecast.

This image makes it clear that an LSTM model outperforms a conventional ARIMA model in producing accurate forecasts for extremely complicated and volatile data, such as wind speed. In contrast to the LSTM, which is better at adapting to and forecasting such difficult data, the ARIMA model's shortcomings in managing fast, non-linear oscillations are glaringly apparent in its smoothed and frequently incorrect predictions.

Based on the comparison of observed data with forecasts from ARIMA and LSTM models across the four meteorological variables (irradiance, temperature, relative humidity, and wind speed). The LSTM model continuously beat the ARIMA model for variables that showed distinct non-linear trends, about changes, or large dynamic swings (most notably, wind speed, relative humidity, and irradiance). The LSTM was able to adjust to shifting patterns and follow the observed data more precisely because of its capacity to grasp intricate non-linear correlations and long-term dependencies. Due to its largely linear nature, the ARIMA model found it difficult to keep up with these dynamic changes, frequently generating flat or excessively smoothed projections that rapidly deviated from the actual values when there was substantial volatility or a shift in the trend.

The visual data indicate that the higher computing costs and complexity of LSTM models are frequently justified for these kinds of meteorological time series. LSTMs provide a notable improvement in forecasting accuracy over conventional linear models in simulations in situations when the data displays nonlinear characteristics.

3.2. Intraday Climate Parameters

Plotting intraday climate parameters within the five Shared Socioeconomic Pathways (SSPs) (SSP 1 - 2.6, SSP 2 - 4.5, SSP 3 - 7.0, SSP 4 - 6.0, SSP 5 - 8.5) is crucial for a comprehensive understanding of future climate change impacts and for informing effective adaptation and mitigation strategies. In order to ensure that future projections appropriately capture local variations and extreme events, it is possible to validate and refine regional climate models and downscaling techniques using intraday climate data, which is available to all SSPs. This is especially crucial as the SSPs show a variety of conceivable futures, and actionable insights depend heavily on the accuracy of models at finer temporal scales.

Figure 4(a) displays the typical daily profile of solar irradiance (in watts per square meter, W/m^2) across 24 hours (hour of day) for five different shared socioeconomic pathways (SSPs). Every one of the five SSPs exhibits a distinct and predictable daily pattern of sun irradiation. At night, when there is no sunshine (from 0:00 to 6:00 and from 19:00 to 24:00), the irradiance is zero. Around six or seven in the morning, when the sun rises, irradiance starts to rise. Approximately 12:00-13:00, or 1 PM, is when it peaks. After that, when the sun sets, it drops throughout the day until it reaches zero once more around 18:00-19:00 (6 - 7 PM). Throughout the day, solar irradiance takes on this bell curve or arch shape.

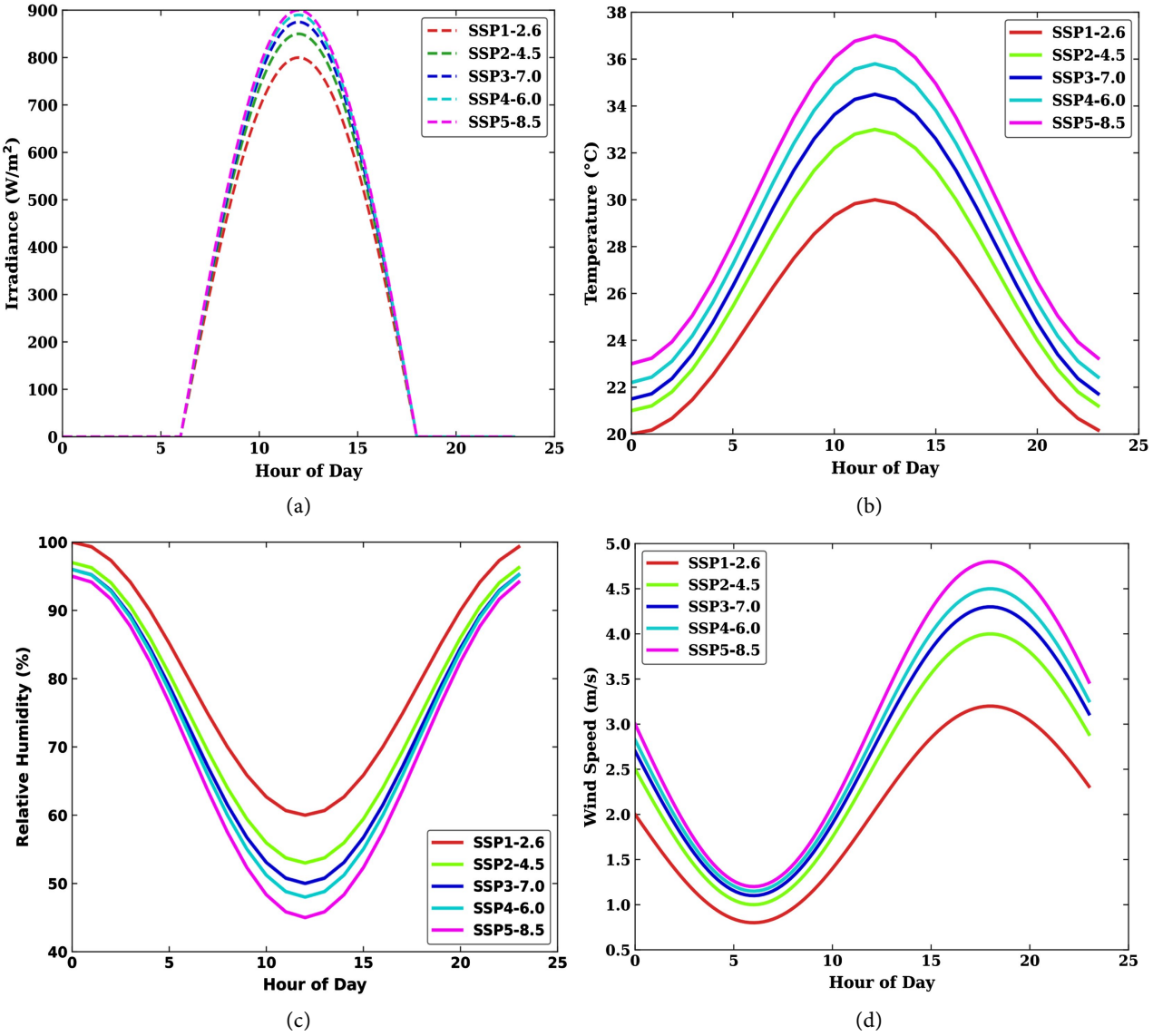

Figure 4. Intraday fluctuation in five scenarios. (a) Intraday solar irradiance; (b) Intraday temperature profile; (c) lntraday relative humidity; (d) Intraday wind speed.

Changes in atmospheric composition, especially aerosol (tiny particles suspended in the atmosphere, such as sulfates, nitrates, dust, and black carbon) con-

centrations, which are implied in the SSP definitions, are probably related to variations in peak sun irradiation among the SSPs.

The graph illustrates how the magnitude of peak irradiance can change across future climatic scenarios, while the basic daily cycle of solar irradiance stays constant. The observed pattern indicates that the underlying assumptions about atmospheric composition (likely aerosol concentrations and/or cloud changes) within these particular SSPs play a significant role, with SSP 5 - 8.5 (highest warming) showing the highest irradiance and SSP 1 - 2.6 (lowest warming) showing the lowest. The potential for solar energy generation, surface warming, and the overall energy balance of the Earth system under various future climatic trajectories are all impacted by this variation in solar irradiance.

Figure 4(b) shows the typical daily temperature variations (in degrees Celsius, ˚C) over 24 hours for five different shared socioeconomic pathways (SSPs). All five SSPs display a typical diurnal (day) temperature cycle. Early in the morning, between 5:00 and 6:00 AM, is when the temperature is at its lowest. The morning and early afternoon saw an increase in temperature. Because heat takes time to gather, temperatures peak in the mid-to-late afternoon (about 14:00-15:00, or 2-3 PM), just after the peak of solar irradiation. Following that, the evening and nighttime temperatures drop.

The basic idea of the shared socioeconomic pathways is immediately reflected in the distinct stratification of temperature profiles: the main cause of these temperature variations is greenhouse gas concentrations, which are expected to rise in the atmosphere under each SSP. Assuming the largest GHG emissions, SSP 5 - 8.5 (fossil-fueled development) produces the most substantial radiative forcing and, thus, the highest temperatures. This is the warmest pathway, as the graph makes evident. Assuming vigorous mitigation measures and low greenhouse gas emissions, SSP 1 - 2.6 (sustainability—taking the green road) produces the least amount of global warming and, as a result, the lowest temperatures portrayed. According to their individual GHG emission paths, the intermediate SSPs (SSP 2 - 4.5, SSP 3 - 7.0, and SSP 4 - 6.0) display matching intermediate temperature profiles. The graph shows the difference in warming between the most pessimistic (SSP 5 - 8.8) and most hopeful (SSP 1 - 2.6) scenarios. There is almost a 7˚C difference in peak temperature between SSP 1 - 2.6 (30˚C) and SSP 5 - 8.5 (37˚C). The minimum temperature difference at night is roughly 4˚C. There are significant distinctions with far-reaching effects. Intraday extremes: The graph shows variations in the average daily temperature as well as variations in peak daytime and minimum nighttime temperatures.

Implications: Comprehending the possible effects of climate change on day-to-day living under many future scenarios requires a comprehension of this graph. It provides immediate information:

- Public health: the risk of heat stress, heatstroke, and mortality.
- Energy demand: the air conditioner's peak electrical demand.
- Agriculture: The impact of heat stress on crop yields.

- Urban planning: the process of creating cooling centers, green areas, and heat-resilient cities.
- Ecosystems: the ability of temperature-sensitive plant and animal species to survive and thrive.

In terms of reducing extreme daily temperatures and the risks that come with them, the variations among the SSPs amply demonstrate the significant advantages of adopting a lower emissions pathway (such as SSP 1 - 2.6).

Generate by providing higher-resolution PDF versions using Times New Roman, bold, for this figure:

Figure 4(c) displays the typical daily profile of relative humidity (in percentage, %) over 24 hours for the five SSPs. All five SSPs exhibit a distinct and predictable inverse relationship between temperature and relative humidity during the day (diurnal cycle). The early morning hours (about 5:00-6:00 AM) have the lowest temperatures and the highest relative humidity. In all cases, the relative humidity is extremely high during these hours, ranging from 95% to 100%. As temperatures climb, relative humidity falls during the morning and early afternoon. Mid-to-late afternoon, approximately 13:00-14:00 or 1-2 PM, is when it reaches its lowest point and typically coincides with the highest temperature. As the temperature drops during the evening and night, it rises again until it reaches high levels in the early morning.

Assuming a comparable level of absolute moisture in the air, the main cause of the observed variations in relative humidity among SSPs is its intrinsic relationship with temperature (although absolute humidity can also change with warming). The amount of water vapor in the air, represented as a percentage of the greatest amount the air can store at a specific temperature, is known as relative humidity. More water vapor can be held by warmer air than by cooler air. The temperature profile graph shows that SSP 5 - 8.5 is the warmest scenario, which means that the air can contain the most moisture. Conversely, SSP 1 - 2.6 is the coolest scenario.

This figure makes it abundantly evident that future climate pathways, particularly warmer ones like SSP 5 - 8.5, are expected to result in noticeably lower daytime relative humidity. Water availability, agricultural output, wildfire risk, and human comfort and health are all significantly impacted by this, underscoring the interdependence of climate factors and the possible difficulties presented by scenarios with increased emissions.

Figure 4(d) presents the typical daily profile of wind speed (in meters per second, m/s) over a 24-hour period for the five SSPs. Wind speed has a distinct and regular diurnal (day) cycle according to all five SSPs: in general, the early morning hours (about 5:00 to 7:00 AM) see the lowest wind speeds. The lowest temperatures and most stable atmospheric conditions frequently occur around this time. Throughout the morning and early afternoon, the wind speed increases. Usually occurring after the peak temperature and when the atmosphere is most unstable due to midday warmth, they peak in the late afternoon or early evening (about

17:00-19:00, or 5 - 7 PM). As the atmosphere settles, wind speeds then drop during the evening and night, reaching their lowest point by the early hours of the morning.

The noteworthy discovery of the wind speed increase from SSP 1 - 2.6 to SSP 5 - 8.5 is probably related to changes in atmospheric energy and stability in a warming climate. Higher temperatures (as shown in the temperature profile for SSP 5 - 8.5) cause more atmospheric instability and convection. Convection is the process by which air rises and becomes less dense when the ground and lower atmosphere warm. Particularly during the day, this increased vertical mixing may result in greater surface winds. Warmer temperatures (especially under SSP 5 - 8.5) indicate that the global climate system has more energy. Higher average wind speeds may result from this enhanced energy, showing up as stronger atmospheric circulation patterns.

Several significant ramifications result from the anticipated rise in intraday wind speeds under higher emissions scenarios: wind energy potential—higher wind speeds may indicate a greater potential for wind power generation, especially during periods of peak demand, which are frequent throughout the day. The frequency and severity of strong wind events must also be taken into account, in addition to normal speeds. Wildfire risk, as demonstrated in the earlier graphics for SSP 5.8 - 5, stronger winds considerably accelerate and intensify the spread of wildfires, posing a larger risk to ecosystems and communities, particularly when paired with higher temperatures and lower relative humidity. Dust storms and soil erosion, especially in arid or agriculturally sensitive areas, higher wind speeds, and drier conditions can exacerbate dust storms and soil erosion.

This graph shows that we can anticipate both higher temperatures and greater daytime winds under future climate scenarios, especially those with higher greenhouse gas emissions (such as SSP 5 - 8.5). This research emphasizes how complex the effects of climate change are and how important it is to take into account all pertinent factors when estimating future risks and creating adaptation plans.

3.3. Impact of Climate Parameters on Perovskite Solar Modules

This section allows us to see the impact of climate variables on solar photovoltaic technologies, especially on perovskite modules.

Figure 5 illustrates how temperature, solar irradiance, and relative humidity, three climate parameters, affect perovskite solar modules' efficiency throughout a day, among other things. Temperature and efficiency: The perovskite module efficiency falls to its lowest point as the temperature rises and peaks around noon. This implies that, like many solar cell technologies, perovskite solar modules may have a negative temperature coefficient, which means that as the temperature rises, their efficiency decreases. Solar irradiance and efficiency: The lowest efficiency is correlated with the highest solar irradiance. According to this figure, high irradiance frequently results in high temperatures (particularly if the modules are not actively cooled), and it is most likely the temperature effect that is reducing effi-

ciency at peak sun hours, even though solar irradiance is required for power generation. Relative humidity and efficiency are at their lowest when relative humidity is at its lowest. Since reduced humidity is typically linked to greater daytime temperatures, this also fits with the temperature trend. Although it's less obvious to conclude that humidity is the reason for the efficiency decline based on this graph alone, it is one of the external factors influencing the modules.

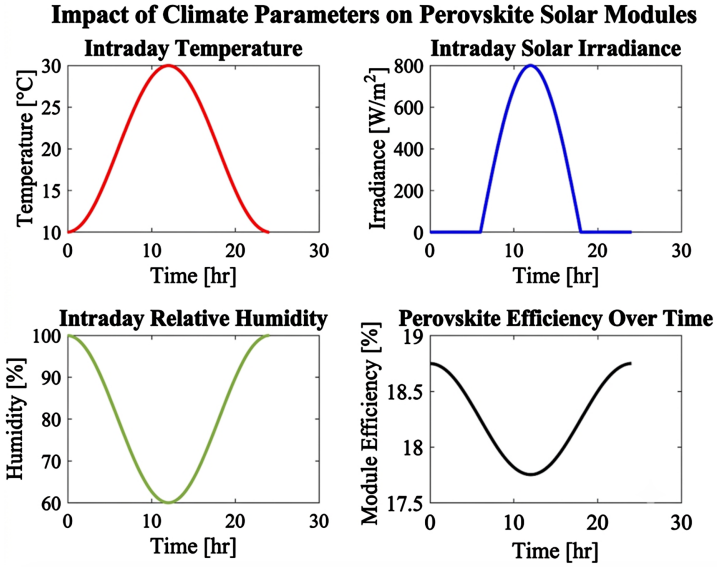

Figure 5. Impact of climate parameters on perovskite solar modules.

This figure illustrates how, although receiving the maximum solar radiation around midday, perovskite solar modules' efficiency actually declines during this time, most likely as a result of the surrounding temperature rising at the same time. This draws attention to a crucial issue facing the implementation of perovskite solar cells: controlling performance in a variety of environmental circumstances, especially high temperatures.

3.4. Sustainable Development Perspective

Figure 6(a) shows five different population projection scenarios from 2020 to 2050, each represented by a distinct shared socioeconomic pathway (SSP).

Among the five scenarios, SSP 1 - 2.6 sustainability (blue line) predicts the slowest population growth. It shows a gradual increase, starting at about 7.8 billion in 2020 and expected to reach around 8.5 billion by 2050. This suggests that effective policies in areas like sustainable development, healthcare, and education will lead to a more stable population and lower fertility rates.

The middle-of-the-road scenario, shown by the SSP 2 - 4.5 Middle of the Road (green line), assumes that economic and societal trends mostly follow historical patterns. By 2050, the global population will be just under 9 billion, up from about 7.8 billion in 2020, at a modest growth rate. This indicates continued progress without the need for drastic sustainability measures or major societal upheavals.

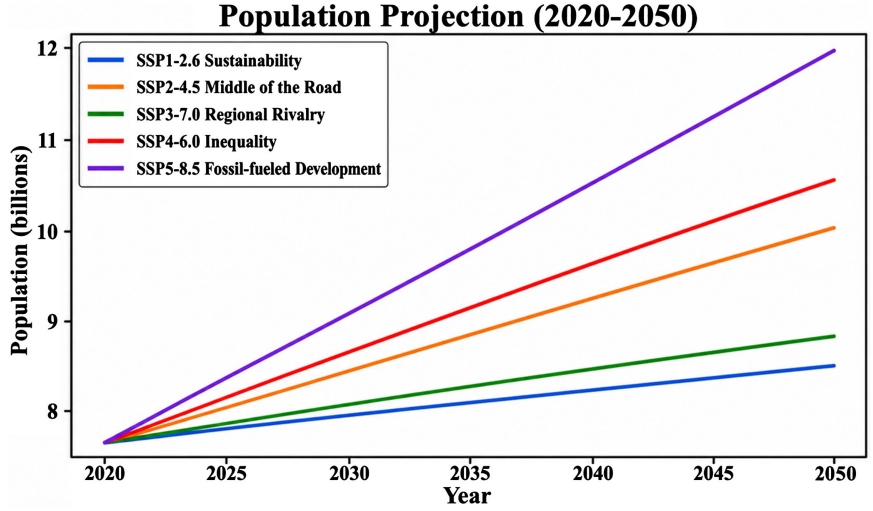

(a)

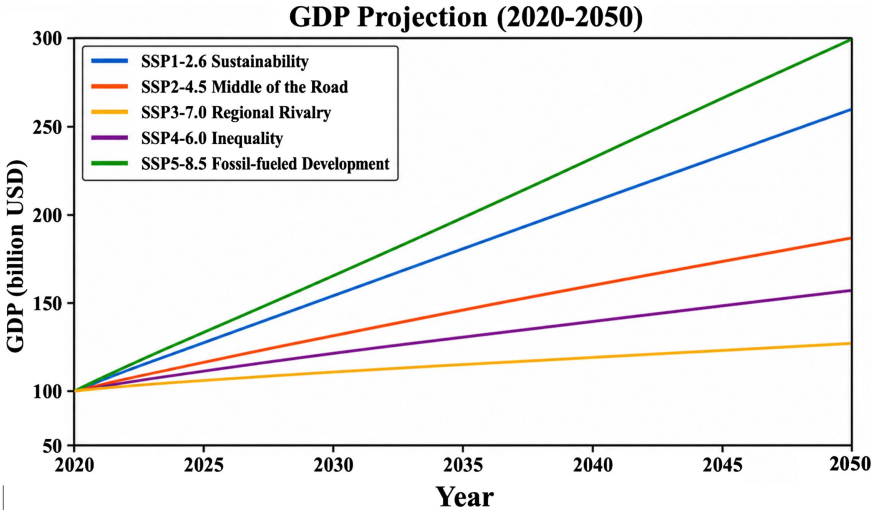

(b)

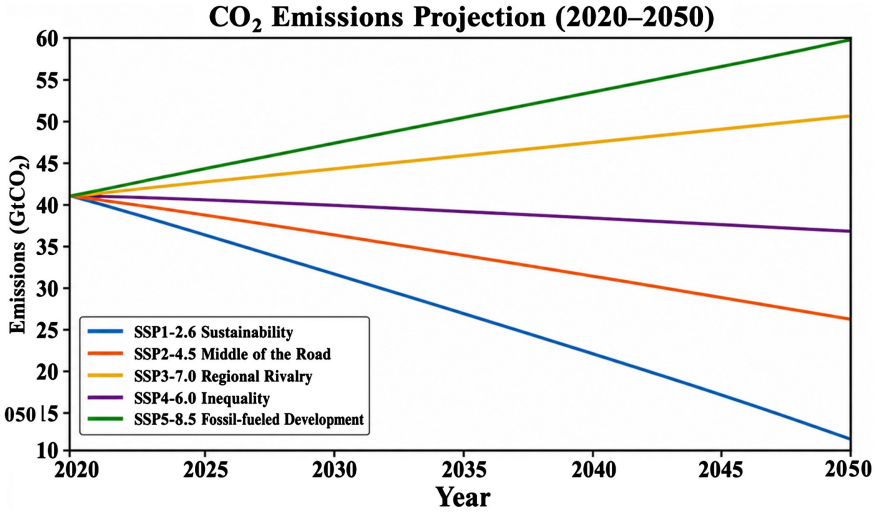

(c)

Figure 6. Sustainable development perspective.

This scenario, SSP 3 - 7.0 regional rivalry (orange line), shows a future characterized by inequality, regional strife, and little international collaboration. By 2050, the population will have grown to almost 10 billion people, faster than in the sustainability and middle-of-the-road scenarios. Higher fertility rates may result from things like less access to healthcare and education.

SSP 4 - 6.0, a future with growing global inequality, where a small elite thrives while a significant section of the population suffers, is depicted by the inequality (purple line) pathway. By 2050, the population is expected to have grown to approximately 10.5 billion. Due to limited access to resources and knowledge, significant inequality frequently results in increased birth rates among underprivileged people.

The future depicted in SSP 5 - 8.5 fossil-fueled development (yellow line) is one marked by a persistent dependence on fossil fuels and fast, resource-intensive economic expansion, frequently at the price of environmental considerations. The population will rise at the fastest rate along this trajectory, from about 7.8 billion in 2020 to over 11.7 billion by 2050. The emphasis on economic growth at the expense of social progress and environmental sustainability may be the cause of this, which could raise fertility rates in some areas.

The world's population is expected to grow between 2020 and 2050 under all five scenarios. The anticipated populations for 2050 show the impact of several socioeconomic pathways on demographic trends, ranging from roughly 8.5 billion (sustainability) to 11.7 billion (fossil-fueled development). Over time, the differences between the scenarios become increasingly noticeable, suggesting that future population size would be significantly impacted by societal changes and policy decisions made in the ensuing decades.

The graph shows how the world's population is expected to change over the next three decades according to various global development trajectories, from sustainable practices to expansion driven by fossil fuels and rising inequality.

Figure 6(b) illustrates five different projections of global gross domestic product (GDP) from the year 2020 to 2050, each corresponding to a different shared socioeconomic pathway (SSP).

Under a sustainability perspective, SSP 1 - 2.6 sustainability (blue line) forecasts robust economic development. The GDP is expected to grow from over 90 trillion USD in 2020 to about 250 trillion USD by 2050. This suggests that achieving sustainable development objectives, like making investments in green technologies, the circular economy, and renewable energy, can result in significant economic growth. According to this route, social justice and environmental preservation can coexist and even promote economic growth.

SSP 2 - 4.5, the middle of the road (orange line), is a scenario of moderate economic growth in which there are no notable shocks or moves toward sustainability, and global development mostly follows historical tendencies. By 2050, GDP will have grown from over 90 trillion USD in 2020 to about 180 trillion USD. This points to a sustained rate of economic growth that is not accelerated.

A future with fragmented global government, more regional disputes, and little international cooperation is portrayed in SSP 3 - 7.0 regional rivalry (yellow line). The economy will develop at the slowest rate of any scenario, from 90 trillion USD in 2020 to only 130 trillion USD by 2050. This demonstrates how protectionist measures, decreased international trade, and geopolitical conflicts may all seriously impede economic growth.

SSP 4 - 6.0, the inequality (purple line) pathway illustrates a future in which economic gains are concentrated within a smaller portion of the population and global inequality is on the rise. By 2050, the total GDP will have grown to over 160 trillion USD, but at a slower rate than in the sustainability or fossil fuel-fueled development scenarios. This implies that overall economic potential may be limited by high levels of inequality, which can result in social instability and underutilization of human capital.

The future depicted in SSP 5 - 8.5 fossil-fueled development (green line) is one of rapid, resource-intensive economic expansion, mostly due to the ongoing use of fossil fuels and focus on GDP maximization at the expense of environmental and social concerns. With a projected increase from 2020 to 2050 of around 190 trillion USD, this path exhibits the fastest GDP growth. This suggests that massive increases in global GDP, at least in the short to medium term, can result from an unbridled pursuit of economic growth, even at the expense of environmental deterioration.

The global GDP is expected to rise between 2020 and 2050 under all five scenarios. From around 130 trillion USD (regional rivalry) to 290 trillion USD (fossil-fueled development), the anticipated GDP for 2050 shows how diverse socioeconomic and policy decisions can result in wildly disparate economic futures. As time goes on, the differences between the scenarios become increasingly noticeable, suggesting that decisions made in the ensuing decades would significantly affect how the world economy develops. Although they do it in very different ways, it is noteworthy that the sustainability (SSP 1 - 2.6) and fossil-fueled development (SSP 5 - 8.5) scenarios both forecast the highest GDP growth, indicating that substantial economic expansion is feasible under opposing development paradigms. But it's crucial to think about each pathway's long-term effects (for example, environmental sustainability for SSP 5 - 8.5).

Figure 6(c) illustrates five different projections of global annual carbon dioxide (CO_2) emissions from 2020 to 2050, each corresponding to a different shared socioeconomic pathway (SSP). All scenarios start around 40 $GtCO_2$ in 2020.

In the SSP 1 - 2.6 sustainability (blue line) scenario, CO_2 emissions are expected to drop significantly and quickly. By 2050, emissions will have decreased from 40 $GtCO_2$ in 2020 to about 10 $GtCO_2$. This course reflects a future in which vigorous climate mitigation measures are put into place, propelled by an international emphasis on sustainability, the uptake of renewable energy, and resource efficiency. In order to keep global warming far below 2˚C, and ideally below 1.5˚C, over preindustrial levels, this is the only viable scenario.

SSP 2 - 4.5 in the middle of the road (orange line) pathway, CO_2 emissions first reduce moderately before declining more slowly. By 2050, emissions will have decreased from 40 $GtCO_2$ in 2020 to about 25 $GtCO_2$. According to this middle-of-the-road scenario, some climate measures are put into place, but they are not bold enough to accomplish significant decarbonization. It depicts a future in which current patterns persist without considerable increases in either climate action or inaction.

The scenario SSP 3 - 7.0 regional rivalry (yellow line) predicts a significant rise in CO_2 emissions. By 2050, emissions will have increased to about 50 $GtCO_2$ from 40 $GtCO_2$ in 2020. With a strong emphasis on regionalism, little international cooperation, and a preference for national security over environmental concerns, this road portrays a fractured globe. Higher emissions result from this absence of concerted climate action.

This approach, known as SSP 4 - 6.0 Inequality (purple line), exhibits a modest initial drop in CO_2 emissions that is followed by a higher level of stabilization. By 2050, emissions level out at about 35 $GtCO_2$, having dropped significantly from 40 $GtCO_2$ in 2020. This scenario depicts a future with growing global inequality in which wealthier countries or groups may pursue environmental legislation, but overall global efforts are impacted by the growing gap between the rich and the poor and a lack of coordinated action.

The scenario that forecasts the largest increase in CO_2 emissions is SSP 5 - 8.5 fossil-fueled development (green line). By 2050, emissions will have increased from 40 $GtCO_2$ in 2020 to roughly 57 $GtCO_2$. This course foresees a future in which the extensive use of fossil fuels will propel economic expansion at a high pace, with little regard for the effects on the environment. This scenario, which results in extremely high levels of global warming, is frequently seen as a business-as-usual or worst-case scenario with regard to climate change.

The graph clearly shows that expected CO_2 emissions vary significantly depending on different socioeconomic and policy choices. Only the SSP 1 - 2.6 sustainability scenario indicates the major reductions in emissions needed to avoid the worst impacts of climate change. According to the SSP 3 - 7.0 and SSP 5 - 8.5 scenarios, there will be considerable global warming in the future as CO_2 emissions continue to rise sharply. The inequality and middle-of-the-road scenario suggest either stabilization or a moderate decline, but not enough to meet the ambitious climate goals.

This graphic highlights the importance of global policy, social development, and energy choices in shaping future CO_2 emission levels and, consequently, the extent of climate change.

Essentially, this data clearly shows that the future is uncertain. Global population trends, economic prosperity, and, most importantly, the planet's climate and environmental health will all be heavily affected by the decisions societies make today about their development paths, including whether to prioritize sustainability, pursue unchecked growth, or become caught up in rivalry and inequality. As

demonstrated by the SSP 1 - 2.6 scenario, achieving truly sustainable development requires integrated actions that simultaneously address social fairness, economic well-being, and environmental conservation.

Figure 7 illustrates the shared socioeconomic projection for Chad from 2020 to 2050 in the context of sustainable development.

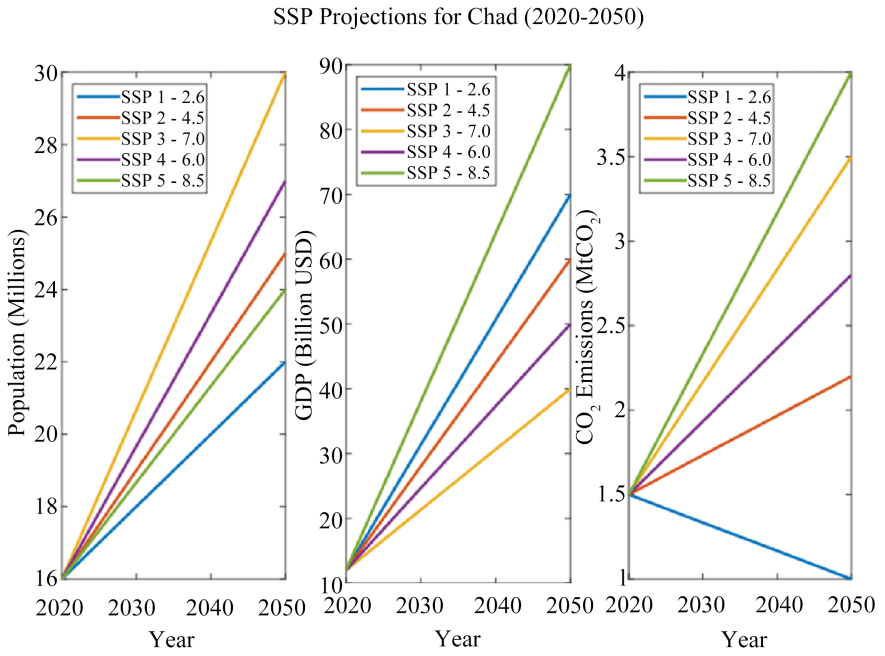

Figure 7. Shared Socioeconomic Pathway (SSP) projection for Chad from 2020 to 2050. (a) Population projection, (b) GDP projection, (c) CO_2 Emissions projection.

These three graphs show Chad's Shared Socioeconomic Pathway (SSP) forecasts for GDP, CO_2 emissions, and population from 2020 to 2050. Each graph displays five distinct SSP scenarios that are appropriate for Chad's particular setting while remaining consistent with the global SSPs previously described.

Figure 7(a), population projection (millions), overall trend, according to all projections, Chad's population is expected to expand significantly between 2020 and 2050. In 2020, the population of Chad was estimated to be 16 million under all circumstances. By 2050, SSP 1 - 2.6 sustainability (blue line) predicts the slowest rate of population growth, with an estimated 22 million people. This suggests that putting more of an emphasis on sustainability may result in things like better family planning, healthcare, and education, which would slow down growth. By 2050, the population in SSP 2 - 4.5, the middle of the road (red line) is expected to rise moderately to around 24 million. This accords with a continuation of present population trends. The largest population growth is predicted by SSP 3 - 7.0 regional rivalry (yellow line), which is expected to reach about 30 million people by 2050. Higher birth rates and rapid population growth may result from issues like restricted access to healthcare and education in a fragmented world with regional conflicts and limited development. SSP 4 - 6.0 by 2050, inequality (the pur-

ple line) will have grown significantly to over 27 million people. Increased birth rates among underprivileged groups are frequently the result of significant inequality. By 2050, the population is expected to rise significantly to approximately 29 million, according to SSP 5 - 8.5 fossil-fueled development (green line). This may be a result of rapid development without adequate family planning or social equality measures.

Figure 7(b) shows the GDP projection (in billion USD) and the overall trend. According to all projections, Chad's GDP will increase significantly from about $10 billion in 2020 to over $70 billion by 2050, especially under SSP 1 - 2.6 sustainability (blue line). This scenario indicates that diversification, green businesses, and better resource management could drive substantial economic growth. The SSP 2 - 4.5 middle-of-the-road projection (red line) forecasts moderate growth to roughly $55 billion, suggesting current economic paths remain steady. The region with the slowest growth, SSP 3 - 7.0 regional rivalry (yellow line), is expected to reach approximately $40 million by 2050, showing how regional instability and lack of cooperation could hamper development. By 2050, SSP 4 - 6.0 inequality (purple line) projects GDP at around $60 billion, reflecting moderate growth that might not be broadly shared due to inequality's effects. The highest growth is predicted by SSP 5 - 8.5 fossil-fueled development (green line), which could surpass $90 billion, implying rapid expansion driven by resource extraction like oil, especially if environmental and social safeguards are weak.

Figure 7(c) shows projected CO_2 emissions ($MtCO_2$) with an overall trend that begins at about 1.5 $MtCO_2$ in 2020. This graph illustrates different trends in Chad's CO_2 emissions. By 2050, SSP 1 - 2.6 sustainability (blue line) predicts that CO_2 emissions will have significantly decreased to around 1 $MtCO_2$. This suggests a future where Chad actively moves toward low-carbon growth, possibly through sustainable agriculture, renewable energy, and improved infrastructure. By 2050, SSP 2 - 4.5 middle of the road (red line) projects emissions will have slightly increased to about 2.2 $MtCO_2$. This indicates that Chad is still developing and making some, though modest, efforts to reduce the impacts of climate change. According to SSP 3 - 7.0 regional rivalry (yellow line), CO_2 emissions are expected to rise sharply, reaching nearly 3.5 $MtCO_2$ by 2050. Higher emissions may be due to a lack of cooperation and prioritizing short-term needs over environmental preservation. SSP 4 - 6.0 inequality (purple line) suggests a moderate increase, with emissions reaching approximately 2.8 $MtCO_2$ by 2050. Even with some progress, the patterns of production and consumption in an unequal society could lead to increased emissions. SSP 5 - 8.5 development fueled by fossil fuels (green line) predicts the fastest growth rate, with emissions reaching about 4 $MtCO_2$ by 2050. This aligns with a development path heavily reliant on fossil fuels and energy.

The future of Chad, like that of the world, depends heavily on the development path chosen, as these data show. In terms of the environment, Chad's sustainability (SSP 1 - 2.6) route is the best because it features declining CO_2 emissions while

supporting strong economic growth and manageable population growth. This suggests Chad can develop sustainably. Conversely, the fossil-fueled development (SSP 5 - 8.5) and regional rivalry (SSP 3 - 7.0) scenarios present serious challenges. Although GDP growth is highest in SSP 5 - 8.5, the country might be forced to pursue a high-carbon development path due to a sharp increase in CO_2 emissions. Reflecting the severe impacts of instability, SSP 3 - 7.0 depicts a bleak outlook of low GDP growth combined with rapid population expansion and increasing emissions. The population estimates show Chad's development concerns; even the most sustainable path still expects a huge population growth, requiring significant efforts to create jobs, infrastructure, and services. The way the graphs interact is quite important. For instance, the SSP 1 - 2.6 scenario for Chad indicates that funding sustainable development might result in a win-win situation for the country's economy and environment. The SSP 5 - 8.5 scenario, on the other hand, indicates a potential trade-off if short-term economic benefits are given precedence over sustainability. It depicts a significant GDP growth but at a substantial environmental cost.

4. Conclusions

Intraday climate fluctuation must be explicitly taken into account in order to comprehend how the new solar system will react to future climate circumstances. This research investigates the effects of sub-daily variations in solar irradiance, ambient temperature, relative humidity, and wind speed on the degradation and performance of perovskite solar modules using a modeling framework.

The analysis verifies that, in the event of future climate change, intraday climate changes will play a crucial role in determining perovskite photovoltaic performance. Temperature and humidity fluctuations over short periods of time increase operational stress and speed up degradation, which lowers energy yield and lifetime. Conventional modeling techniques based on daily or monthly climate averages underestimate these effects. Predictive accuracy is increased, and more thorough techno-economic and sustainability assessments are supported when high-resolution climatic dynamics are integrated into photovoltaic performance evaluation. The suggested paradigm influences investment and policy choices targeted at long-term sustainable development and aids in the creation of robust solar energy systems.

Acknowledgements

This work was funded by the Partnership for Applied Skills in Sciences, Engineering, and Technology—Regional Scholarship and Innovation Fund (PASET-RSIF) and the Carnegie Corporation of New York.

Credit Authorship Contribution Statement

Wakiang Emile Latchiba: writing the original draft, conducting formal analyses, developing software, establishing methodologies, creating visualizations, validat-

ing results, conceptualizing, and performing investigations. **Sebastian Waita:** writing review and providing editing supervision. **Robert Krueger:** writing review and providing editing supervision. **Julius M. Mwabora:** writing review and providing editing supervision.

Conflicts of Interest

The following financial and personal relationships are disclosed by the authors and could be viewed as possible conflicts of interest:

Wakiang Emile Latchiba's report was provided by the Partnership for Applied Sciences, Engineering, and Technology (PASET)-Regional Scholarship and Innovation Fund (RSIF) and the Carnegie Corporation of New York. If there are other authors, they declare that they have no known competing financial interests or personal relationships that could be perceived as influencing the work presented in this paper.

Data Accessibility

The corresponding author can provide the datasets used and/or analyzed in the current work upon reasonable request.

References

[1] Stoichkov, V., Bristow, N., Troughton, J., De Rossi, F., Watson, T.M. and Kettle, J. (2018) Outdoor Performance Monitoring of Perovskite Solar Cell Mini-Modules: Diurnal Performance, Observance of Reversible Degradation and Variation with Climatic Performance. *Solar Energy*, **170**, 549-556. https://doi.org/10.1016/j.solener.2018.05.086

[2] Lipovšek, B., Jošt, M., Tomšič, Š. and Topič, M. (2022) Energy Yield of Perovskite Solar Cells: Influence of Location, Orientation, and External Light Management. *Solar Energy Materials and Solar Cells*, **234**, Article 111421. https://doi.org/10.1016/j.solmat.2021.111421

[3] Gehlhaar, R., Merckx, T., Qiu, W. and Aernouts, T. (2018) Outdoor Measurement and Modeling of Perovskite Module Temperatures. *Global Challenges*, **2**, Article No. 1800008. https://doi.org/10.1002/gch2.201800008

[4] Mavlonov, A., Hishikawa, Y., Kawano, Y., Negami, T., Hayakawa, A., Tsujimura, S., *et al.* (2024) Thermal Stability Test on Flexible Perovskite Solar Cell Modules to Estimate Activation Energy of Degradation on Temperature. *Solar Energy Materials and Solar Cells*, **277**, Article 113148. https://doi.org/10.1016/j.solmat.2024.113148

[5] Mavlonov, A., Hishikawa, Y., Kawano, Y., Negami, T., Hayakawa, A. and Minemoto, T. (2025) Investigating the Stability of Flexible Perovskite Solar Cell Modules in Heat and Damp-Heat Environments. *Solar Energy Materials and Solar Cells*, **282**, Article 113410. https://doi.org/10.1016/j.solmat.2025.113410

[6] Kato, Y., Katayama, H., Kobayashi, T., Kozawa, M., Nishigaki, Y., Kobayashi, T., *et al.* (2022) Global Prediction of the Energy Yields for Hybrid Perovskite/Si Tandem and Si Heterojunction Single Solar Modules. *Progress in Photovoltaics: Research and Applications*, **30**, 1198-1218. https://doi.org/10.1002/pip.3569

[7] Bhandari, S., Ghosh, A., Roy, A., Mallick, T.K. and Sundaram, S. (2022) Compelling Temperature Behaviour of Carbon-Perovskite Solar Cell for Fenestration at Various

Climates. *Chemical Engineering Journal Advances*, **10**, Article 100267. https://doi.org/10.1016/j.ceja.2022.100267

[8] Tewari, C., Tatrari, G., Kumar, S., Pandey, S., Rana, A., Pal, M., *et al.* (2022) Green and Cost-Effective Synthesis of 2D and 3D Graphene-Based Nanomaterials from Drepanostachyum Falcatum for Bio-Imaging and Water Purification Applications. *Chemical Engineering Journal Advances*, **10**, Article 100265. https://doi.org/10.1016/j.ceja.2022.100265

[9] Kling, M.M., Baer, K.C. and Ackerly, D.D. (2024) A Tree's View of the Terrain: Downscaling Bioclimate Variables to High Resolution Using a Novel Multi-Level Species Distribution Model. *Ecography*, **2024**, e07131. https://doi.org/10.1111/ecog.07131

[10] Guo, J., Jia, H., Wang, Y., Wang, X. and Li, W. (2024) Dynamical Downscaling of Daily Extreme Temperatures over China Using PRECIS Model. *Sustainability*, **16**, Article 3030. https://doi.org/10.3390/su16073030

[11] Bonato, M., Cepni, O., Gupta, R. and Pierdzioch, C. (2023) Climate Risks and Realized Volatility of Major Commodity Currency Exchange Rates. *Journal of Financial Markets*, **62**, Article 100760. https://doi.org/10.1016/j.finmar.2022.100760

[12] Zhou, Y., Liang, Z., Li, B., Huang, Y., Wang, K. and Hu, Y. (2021) Seamless Integration of Rainfall Spatial Variability and a Conceptual Hydrological Model. *Sustainability*, **13**, Article 3588. https://doi.org/10.3390/su13063588

[13] Singh, S. and Goyal, M.K. (2023) Enhancing Climate Resilience in Businesses: The Role of Artificial Intelligence. *Journal of Cleaner Production*, **418**, Article 138228. https://doi.org/10.1016/j.jclepro.2023.138228

[14] Plavcová, L., Tumajer, J., Altman, J., Svoboda, M., Stegehuis, A.I., Pejcha, V., *et al.* (2025) High Inter-Specific Diversity and Seasonality of Trunk Radial Growth in Trees along an Afrotropical Elevational Gradient. *Plant, Cell & Environment*, **48**, 2285-2297. https://doi.org/10.1111/pce.15295

[15] Alizadeh, O. (2022) Advances and Challenges in Climate Modeling. *Climatic Change*, **170**, Article No. 18. https://doi.org/10.1007/s10584-021-03298-4

[16] Chakraborty, D., Alam, A., Chaudhuri, S., Başağaoğlu, H., Sulbaran, T. and Langar, S. (2021) Scenario-Based Prediction of Climate Change Impacts on Building Cooling Energy Consumption with Explainable Artificial Intelligence. *Applied Energy*, **291**, Article 116807. https://doi.org/10.1016/j.apenergy.2021.116807

[17] Xu, Z., Chen, L., Qin, P. and Ji, X. (2023) Projection and Uncertainty Analysis of Future Temperature Change over the Yarlung Tsangpo-Brahmaputra River Basin Based on Cmip6. *Water*, **15**, Article 3595. https://doi.org/10.3390/w15203595

[18] Aryal, S., Grießinger, J., Dyola, N., Gaire, N.P., Bhattarai, T. and Bräuning, A. (2023) INTRAGRO: A Machine Learning Approach to Predict Future Growth of Trees under Climate Change. *Ecology and Evolution*, **13**, e10626. https://doi.org/10.1002/ece3.10626

[19] Tomšič, Š., Jošt, M., Brecl, K., Topič, M. and Lipovšek, B. (2023) Energy Yield Modeling for Optimization and Analysis of Perovskite-Silicon Tandem Solar Cells under Realistic Outdoor Conditions. *Advanced Theory and Simulations*, **6**, Article No. 2200931. https://doi.org/10.1002/adts.202200931

[20] Zhao, Y. and Liu, S. (2023) Effects of Climate Change on Economic Growth: A Perspective of the Heterogeneous Climate Regions in Africa. *Sustainability*, **15**, Article 7136. https://doi.org/10.3390/su15097136

[21] Liu, J., Ma, X., Duan, Z., Jiang, J., Reichstein, M. and Jung, M. (2020) Impact of Tem-

poral Precipitation Variability on Ecosystem Productivity. *WIREs Water*, **7**, e1481. https://doi.org/10.1002/wat2.1481

[22] Carvalho, D., Cardoso Pereira, S. and Rocha, A. (2021) Future Surface Temperatures over Europe According to CMIP6 Climate Projections: An Analysis with Original and Bias-Corrected Data. *Climatic Change*, **167**, Article No. 10. https://doi.org/10.1007/s10584-021-03159-0

[23] Shu, Q., Wang, Q., Årthun, M., Wang, S., Song, Z., Zhang, M., *et al.* (2022) Arctic Ocean Amplification in a Warming Climate in CMIP6 Models. *Science Advances*, **8**, eabn9755. https://doi.org/10.1126/sciadv.abn9755

[24] Opoku, S.K., Filho, W.L., Hubert, F. and Adejumo, O. (2021) Climate Change and Health Preparedness in Africa: Analysing Trends in Six African Countries. *International Journal of Environmental Research and Public Health*, **18**, Article 4672. https://doi.org/10.3390/ijerph18094672

[25] Zhu, X., Qu, F., Fan, R., Chen, Z., Wang, Q. and Yu, G. (2022) Effects of Ecosystem Types on the Spatial Variations in Annual Gross Primary Productivity over Terrestrial Ecosystems of China. *Science of The Total Environment*, **833**, Article 155242. https://doi.org/10.1016/j.scitotenv.2022.155242

[26] Maclean, I.M.D. (2019) Predicting Future Climate at High Spatial and Temporal Resolution. *Global Change Biology*, **26**, 1003-1011. https://doi.org/10.1111/gcb.14876

[27] Tebaldi, C., Debeire, K., Eyring, V., *et al.* (2021) Climate Model Projections from the Scenario Model Intercomparison Project (ScenarioMIP) of CMIP6. *Earth System Dynamics*, **12**, 253-293.

[28] Dosio, A., Jury, M.W., Almazroui, M., Ashfaq, M., Diallo, I., Engelbrecht, F.A., *et al.* (2021) Projected Future Daily Characteristics of African Precipitation Based on Global (CMIP5, CMIP6) and Regional (CORDEX, CORDEX-CORE) Climate Models. *Climate Dynamics*, **57**, 3135-3158. https://doi.org/10.1007/s00382-021-05859-w

[29] Liu, J., He, Y., Ding, L., Zhang, H., Li, Q., Jia, L., *et al.* (2024) Perovskite/Silicon Tandem Solar Cells with Bilayer Interface Passivation. *Nature*, **635**, 596-603. https://doi.org/10.1038/s41586-024-07997-7

[30] Hou, Y., Aydin, E., De Bastiani, M., Xiao, C., Isikgor, F.H., Xue, D., *et al.* (2020) Efficient Tandem Solar Cells with Solution-Processed Perovskite on Textured Crystalline Silicon. *Science*, **367**, 1135-1140. https://doi.org/10.1126/science.aaz3691

[31] Eyring, V., Bony, S., Meehl, G.A., Senior, C.A., Stevens, B., Stouffer, R.J., *et al.* (2016) Overview of the Coupled Model Intercomparison Project Phase 6 (CMIP6) Experimental Design and Organization. *Geoscientific Model Development*, **9**, 1937-1958. https://doi.org/10.5194/gmd-9-1937-2016

[32] Blazakis, K., Schetakis, N., Bonfini, P., Stavrakakis, K., Karapidakis, E. and Katsigiannis, Y. (2024) Towards Automated Model Selection for Wind Speed and Solar Irradiance Forecasting. *Sensors*, **24**, Article 5035. https://doi.org/10.3390/s24155035

[33] Xu, D., Zhang, Q., Ding, Y. and Zhang, D. (2022) Application of a Hybrid ARIMA-LSTM Model Based on the SPEI for Drought Forecasting. *Environmental Science and Pollution Research*, **29**, 4128-4144. https://doi.org/10.1007/s11356-021-15325-z

[34] Chen, H., Su, Z. and Xing, Z. (2024) Forecasting Extreme High Temperatures Based on an ARIMA-LSTM Hybrid Model. 2024 *IEEE* 2*nd International Conference on Image Processing and Computer Applications* (*ICIPCA*), Shenyang, 28-30 June 2024, 804-809. https://doi.org/10.1109/icipca61593.2024.10709045